PUBLICATIONS OF THE ASTRONOMICAL SOCIETY OF THE PACIFIC, **115**:712–719, 2003 June

The Four-Quadrant Phase Mask Coronagraph. III. Laboratory Performance

P. RIAUD, A. BOCCALETTI, J. BAUDRAND, AND D. ROUAN

LESIA, Observatoire de Paris-Meudon, 5 Place Jules Janssen, F-92195 Meudon, France; pierre.riaud@obspm.fr, jacques.baudrand@obspm.fr, anthony.boccaletti@obspm.fr, daniel.rouan@obspm.fr.

Received 2003 January 9; accepted 2003 March 3

ABSTRACT. We report a laboratory experiment to assess the performance and limitations of the four-quadrant phase mask coronagraph we proposed 2 years ago. A total flux rejection factor of 4400 was reached using off-the-shelf optical components. The peak intensity of the Airy pattern is correspondingly reduced by a factor of 44,000 with a stability of a few hours. In this paper, we discuss implications of this excellent result regarding the next generation of instruments for extrasolar planet detection.

1. INTRODUCTION

Back in 1939, B. Lyot first proposed using an opaque mask in the focal plane of a telescope to improve the contrast of solar observations (Lyot 1939). This coronagraph proved to be very efficient for systematic observations of the solar corona and was later turned into a stellar coronagraph to search for faint materials around bright stars such as circumstellar disks or low-mass companions. However, the stellar Lyot coronagraph does not perform well enough (in terms of angular separation) to allow a more ambitious program: the direct detection of extrasolar planets.

More recently, new concepts of high-contrast coronagraphs have been investigated, and in particular, Roddier & Roddier (1997) have proposed to use a phase mask instead of an amplitude mask. This device provides a π phase shift of half of the focal spot, resulting in a self-destructive interference in the relayed pupil. As for the Lyot coronagraph, an appropriate stop is then inserted into the pupil plane to block the starlight, which is spread out of the geometric pupil.

The disk phase mask is totally transparent and is also much smaller than a Lyot mask, allowing high-contrast imaging closer to the star.

Nevertheless, the disk phase mask is highly chromatic regarding both the phase shift and the mask size ($\sim 0.5\lambda/D$). Rouan et al. (2000) solved the mask size wavelength dependence by turning the disk phase mask into a four-quadrant phase mask (FQPM). The concept and expected performance of the FQPM have been fully described in Rouan et al. (2000) and Riaud et al. (2001). It has been demonstrated that for a circular pupil without any aberration, the starlight attenuation is mathematically null (Rouan, Riaud, & Baudrand 2002).

In more realistic conditions, the performance of any coronagraph is always much worse than in the perfect case. Phase-mask coronagraphs are indeed very sensitive to several factors: pupil shape, chromatism, wave-front distortions, residual jitter, and manufacturing accuracy of the mask. For instance, Guyon et al. (1999) have reported an attenuation factor of about 16 using a disk phase mask in a lab experiment.

In this paper, we present a laboratory experiment to address the performance of an FQPM prototype. Section 2 describes the FQPM manufacturing process, and § 3 shows the optical setup of the coronagraphic bench to test the phase mask. Some laboratory results obtained in monochromatic light are presented in § 4, and we discuss the main limitations in §§ 5 and 6, as well as future developments in § 7.

2. THE FQPM MANUFACTURING

The FQPM prototype in transmission was manufactured by SAGEM/REOSC. The $\lambda/2$ retardation between quadrants is provided by a layer of alumina (Al_2O_3) evaporated onto a polished substrate of glass. The alumina has good mechanical properties and is chemically inert. However, this alumina layer features an important porosity, and therefore the refraction index is only $n = 1.59$–1.6 instead of $n = 1.76$ for the bulk material. The refraction index of the glass substrate is chosen to be close to the index of alumina (Corning glass C2036 with $n = 1.616$ at 632.8 nm) in order to reduce unwanted interferences between the glass and the alumina. An antireflection coating (0.15%) has been deposited onto the back side to limit ghost-image pollution.

2.1. The "Lift-off" Process

The quadrants geometry is obtained by the "lift-off" technique. This process is performed through five sequential steps, which are as follows:

1. deposition of a photosensitive resin layer on the C2036 substrate,
2. ultraviolet illumination through a photolithographic four-quadrant mask,
3. resin development and removal of exposed resin,

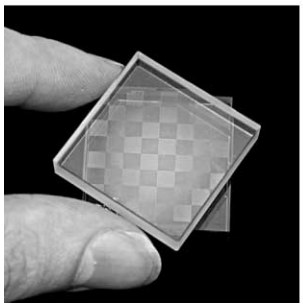

FIG. 1.—Image of the multi-FQPM manufactured by SAGEM and tested with polychromatic interferences.

4. deposition of Al_2O_3, and
5. chemical removal of the unexposed resin layer plus its Al_2O_3 overcoating.

2.2. Mask Specifications

To obtain a π phase shift between quadrants, the thickness of the step is given by the relation

$$2(n - 1)e = \lambda, \quad (1)$$

where n is the refraction index of alumina ($n = 1.59$–1.60) and λ is the wavelength of a monochromatic source. Instead of manufacturing a single FQPM, SAGEM has provided us with a substrate supporting an array of 49 individual masks, each with an area of 49 mm^2 (Fig. 1).

For one of these masks, a thin chromium cross (10 μm in width) was deposited on the mask to avoid some nulling degradation induced by the imperfect quadrant transition. This mask was used to obtain the results presented in this article. The alumina thickness was measured by SAGEM to be 533.3 $\pm$ 1 nm and designed to operate at a wavelength of 640 $\pm$ 0.8 nm. The substrate specifications are listed in Table 1.

TABLE 1
OPTICAL SPECIFICATIONS OF THE CORNING C2036 SUBSTRATE

Parameter	Value
Size	30 × 30 × 6 mm
Index of refraction	$n = 1.616$ at 632.8 nm
Parallelism	≈15″
Polish on the whole surface	λ/25 PTV or λ/100 rms
Polish on a single FQPM	λ/37 PTV or λ/190 rms
Roughness	≈0.8 nm

3. OPTICAL SETUP

The optical layout of the experiment is shown in Figure 2. The light source is a monochromatic ($\Delta\lambda = 2$ nm) pigtail laser diode adjustable from 630 to 640 nm according to its temperature. The diameter of the single mode fiber is 4 μm. The first lens (L1) is projecting the image of the source at infinity, and the parallel beam (25 mm in diameter) is stopped down by the entrance pupil (1.7 mm diameter) located at the image focus of L1. A second lens (L2) focuses the beam to form an Airy pattern on the FQPM device. At this focus, the image quality is very good (< λ/10 peak to valley [PTV]) and several Airy rings can be seen.

The FQPM is mounted on x, y, z stages with an accuracy of 1 μm for x and y and 10 μm for the z-axis (focus). In this configuration, the f-number is 265 and the size (λ/D) of the Airy pattern projected onto the mask is 169 μm at $\lambda = 640$ nm. The lens L3 conjugates the entrance pupil with the Lyot stop to filter out the coronagraphic diffraction at the edge of the pupil. The focal ratio between L2 and L3 gives a reduction factor of the pupil image by 3.91 providing a relayed pupil of 435 μm in diameter. The Lyot stop is a simple pinhole of

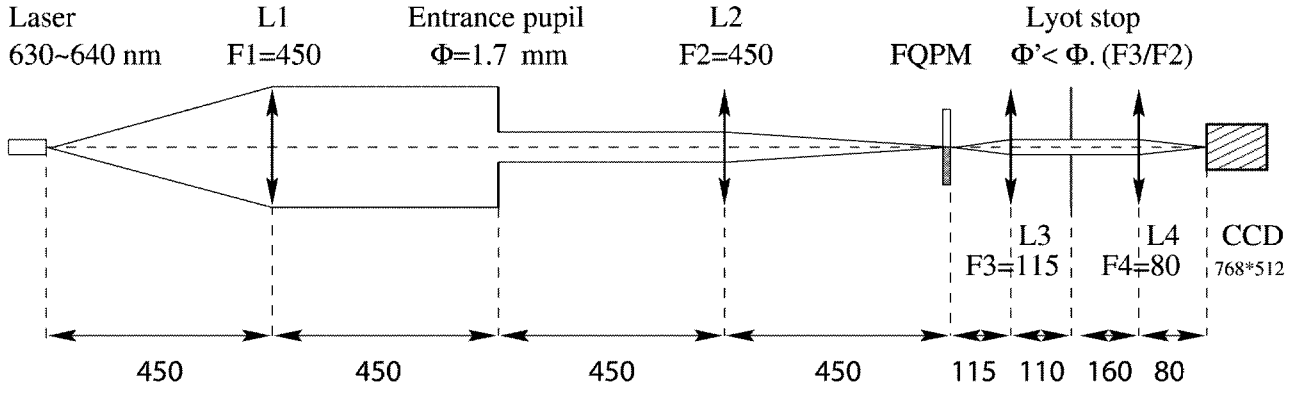

FIG. 2.—Optical layout of the FQPM coronagraph experiment. The entrance pupil is a hole of 1.7 mm in diameter. The lenses L1, L2, and L3 are made with fused silica and feature a standard polish of λ/10 PTV at 632.8 nm. The lenses L2 and L3 include antireflection coatings on the two faces ($R < 0.15\%$ each). The Lyot stop is a pinhole 320 μm in diameter (74% of the pupil size). The CCD camera (768 × 512 pixels KAF 400 chip) is recording the coronagraphic images. All distances are in millimeters.

320 μm in diameter designed to undersize the pupil by about 26%. It is also mounted on *x*, *y*, *z* stages with an accuracy of 10 μm.

The last lens (L4) is a simple achromat forming the coronagraphic image onto the camera, a KAF 400 CCD chip cooled by one Peltier module (−15°C). The pixel size of 9 × 9 μm yields a large sampling of 15 pixels per λ/D.

4. LABORATORY RESULTS

4.1. Acquisition and Data Processing

The power of the laser diode varies from 0.05 to 15 mW. The exposure time of coronagraphic images is typically 1 s for 15 mW. To avoid the saturation of noncoronagraphic images, we used a neutral density and shorter exposures (0.25 s). The MTO S2608 neutral density has been calibrated with a silicon diode detector and was found to provide an attenuation factor of $(5.1 \pm 0.1) \times 10^3$. A series of about 20 coronagraphic images is then recorded and subtracted with a median dark frame (derived from five individual darks). To infer the rejection factor, we compare the flux of coronagraphic images with the flux of off-axis images (noncoronagraphic) with appropriate scaling (integration time and density).

4.2. Operating Wavelength

The FQPM is manufactured for an optimal wavelength, which has to be accurately determined. For that purpose, we implemented on the optical bench a low-resolution spectroscopic device to disperse the coronagraphic image and hence derive the operating wavelength. A transmission grating (110 lines mm^{-1}) with about 25% of transmission in the first order was used to obtain a pixel sampling of about 0.26 nm on the CCD between 500 and 800 nm. The wavelength calibration is performed on the He-Ne laser line at 632.8 nm and the sodium yellow lines at 589 and 589.6 nm. We first acquire a coronagraphic image with a white halogen lamp at 3400 K with a long exposure time (30–120 s). Then a direct image is recorded without the coronagraphic mask (off-axis image) and a shorter exposure time (1–5 s). These two spectra are then divided to derive the wavelength dependence of the rejection factor. The spectroscopic measurement of the SAGEM's mask is displayed in Figure 3. The maximum rejection is obtained at 628 ± 1 nm, and the spectral profile follows a parabolic behavior as expected (Rouan et al. 2002). This result is slightly different from the initial value given by SAGEM (640 nm). Actually, we later realized that the alumina layer was porous, which causes a variation of the optimal wavelength according to the room conditions (temperature, humidity, dust, etc.). We measured operating wavelengths as large as 651 nm when the mask was cleaned with alcohol, as shown in Figure 3.

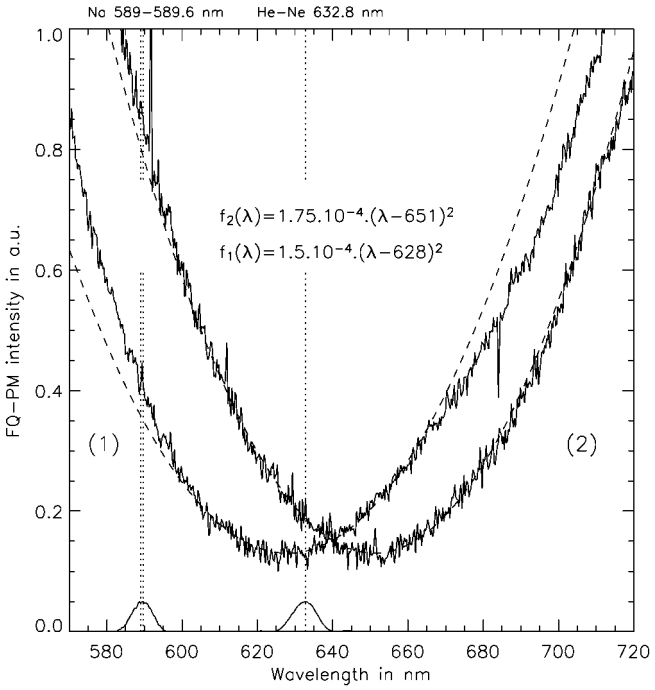

FIG. 3.—Low-resolution spectroscopy of a coronagraphic image to determine accurately the mask operating wavelength. The spectral calibration is performed on three references lines (He-Ne laser at 632.8 nm and sodium yellow lines 589–589.6 nm). The wavelength dependence is close to a power square law as predicted by theory (see eq. [9]). The maximum rejection occurs at 628 ± 1 nm, thus defining the operating wavelength (1). A cleaning of the mask increases the optical index and shifts the operating wavelength to 651 nm (2).

4.3. Rejection Factor

We first obtained an image of the coronagraphic pupil to demonstrate that the prototype performance was in agreement with theoretical work (Riaud et al. 2001). Figure 4*a* shows an attenuated geometric pupil surrounded with a bright diffraction pattern. The smaller Lyot stop is then mandatory to remove this stellar light. However, the optical system not being perfect, a significant amount of light is not canceled by the coronagraph and still remains in the final focal plane (Fig. 4*b*). The prototype performance is directly measured on this coronagraphic image. We compared the total energy contained in $24\lambda/D \times 24\lambda/D$ on the coronagraphic image with the noncoronagraphic image to derive a total rejection factor of 4400 ± 200. We also obtained a peak attenuation of 44,000 ± 2000, comparing the brightest residuals to the point-spread function (PSF) peak. Azimuthally averaged profiles of the coronagraphic images are presented in Figures 5 and 6. A few bright features limiting the detectivity can be identified in Figure 4*b*. First of all, a cross composed of speckles appears on the image diagonals. This feature is a diffraction pattern originating from the transition between the mask quadrants. Second, a large halo slightly shifted from the center (lower left) is caused by a ghost image

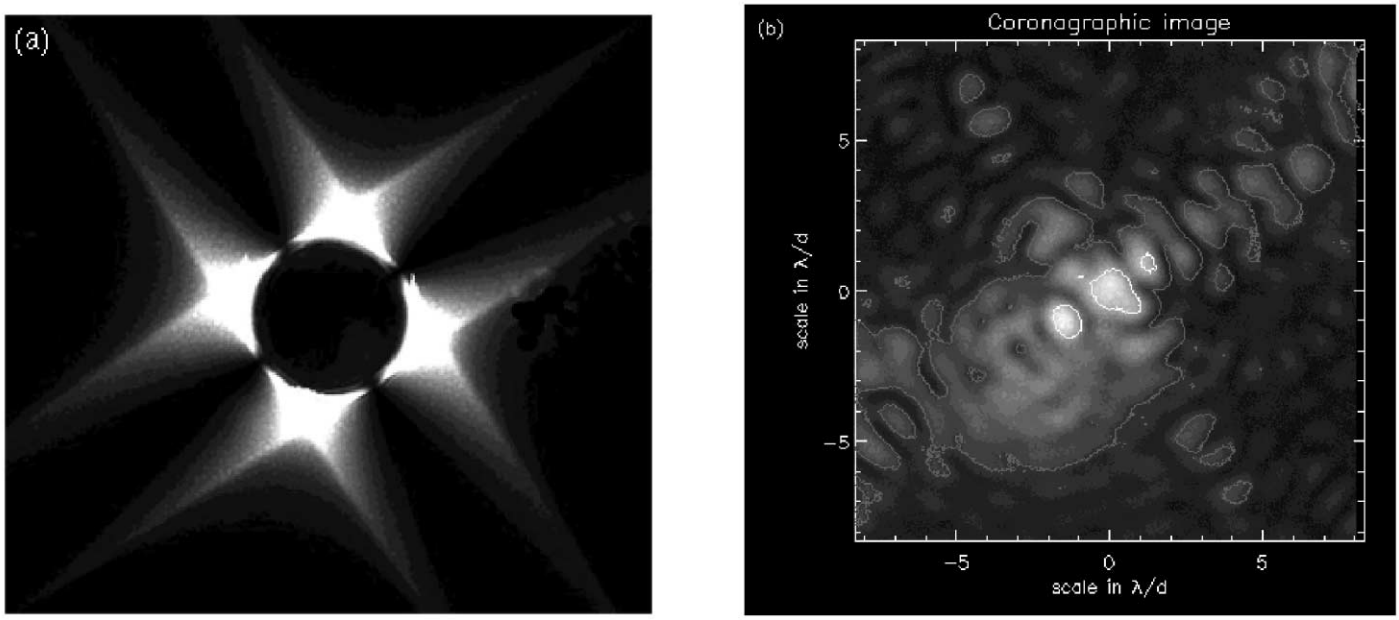

FIG. 4.—(*a*) Effect of the FQPM coronagraph on the pupil. (*b*) Coronagraphic residuals after spatial filtering by the Lyot stop. The overplotted contours correspond to 10^{-5} and 10^{-6} levels with respect to the stellar peak.

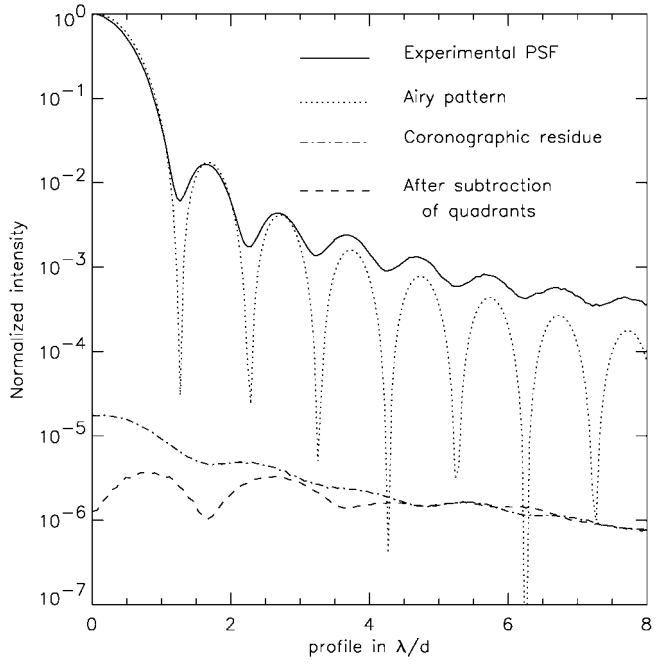

FIG. 5.—Normalized radial profiles obtained for the experimental PSF (*solid line*), the theoretical Airy pattern (*dotted curve*), and the coronagraphic residuals of Fig. 4*b* before and after centrosymmetrical subtraction. Curves are azimuthally averaged.

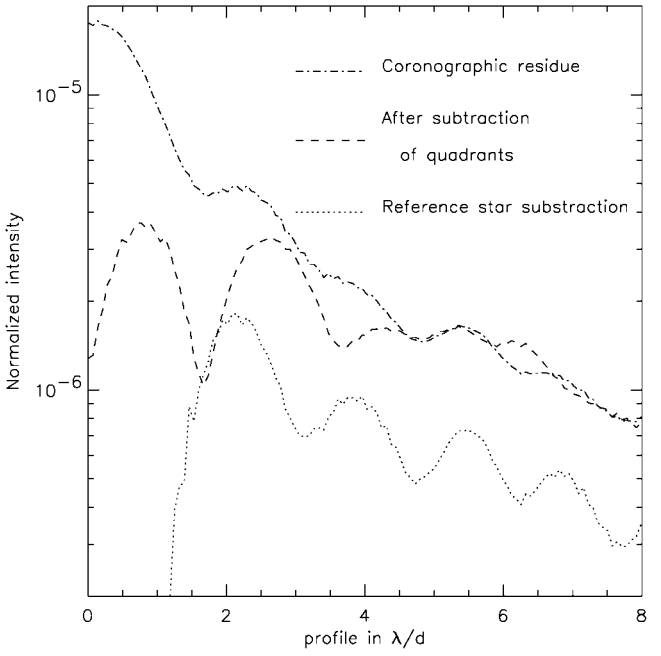

FIG. 6.—Magnification of Fig. 5. The dash-dotted line shows the coronagraphic profile, and we compare the centrosymmetrical subtraction (*dashed line*) with the reference star subtraction (*dotted line*) obtained 2 days later. The residual image is definitely not centrosymmetrical since the reference star subtraction yields a significant improvement in contrast (a factor of 2–3) beyond $2\lambda/D$. Curves are azimuthally averaged.

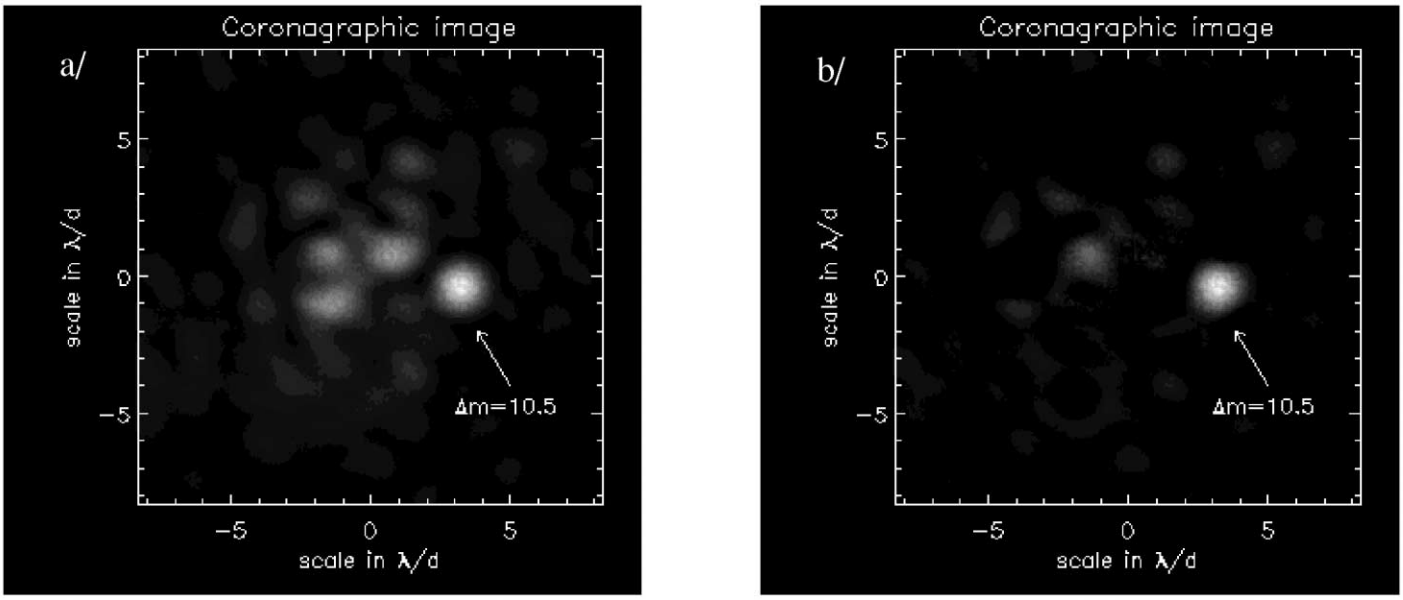

FIG. 7.—Artificial companion ($\Delta M = 10.5$ at $3.6\lambda/D$) is added to the coronagraphic residuals. Here the rejection factor is lower than our best result. The speckle level is increased with respect to Fig. 4*b* since the companion image is obtained with a double reflection on a imperfect parallel plate. The images are composed of 16 individual frames. The companion is detected at (*a*) 17 σ and (*b*) 23 σ after centrosymmetrical subtraction.

despite an excellent antireflection coating of the L3 lens. Finally, the stellar peak is also not perfectly attenuated for several reasons detailed in § 5.

4.4. Detection Capability

Once the total rejection factor and the star peak attenuation were calculated, we also assessed the detection capability for an off-axis companion located at a few Airy rings from the star. The image of the companion is obtained with a double reflection on a parallel plate. Three different star/companion ratios can be obtained. With a double vitreous reflection, the luminosity ratio is 330 ($\Delta M = 6.3$). If the plate is antireflection coated on one face, the ratio is 15,000 ($\Delta M = 10.5$). With an antireflection coating on each face, the ratio reaches 660,000 ($\Delta M = 14.5$). According to the result presented in § 4.3, the fainter companion ($\Delta M = 14.5$) could have been detected. However, the imperfect parallel plate significantly increases the residual speckles by about a factor of 2, and the stellar peak attenuation factor is markedly reduced to 22,000 instead of 44,000. Nevertheless, we were able to detect the $\Delta M = 10.5$ companion located at $3.6\lambda/D$ from the center. As shown in Figure 7, the companion appears 17 times brighter than the speckle residuals in Figure 7*a* and 23 times brighter thanks to the centrosymmetrical subtraction (Fig. 7*b*; see Boccaletti, Riaud, & Rouan 2002 for a discussion of this property). A $\Delta M \approx 12$ companion would have been detected at 5 σ in this experiment.

4.5. Stability

We have also been interested in the temporal stability of the coronagraphic device. We performed a series of five coronagraphic exposures and five individual dark frames during a single day. The photometric measurements have an accuracy of about 5% PTV. The rejection factor does not deviate by more than 5% from the initial measurement in 7 hr, thus demonstrating the very good stability of the optical bench itself.

5. PERFORMANCE LIMITATION

5.1. Wavelength Considerations

The mask being manufactured for a given wavelength (λ_0), the use of a spectral bandwidth ($\Delta\lambda$) degrades the rejection factor. At the operating wavelength ($\lambda = \lambda_0$), the complex quantity in the focal plane (a) is divided in two equal parts with opposite signs ($\pm a/2$), as a result of the π phase shift, and is therefore perfectly nulled in the relayed pupil. For an arbitrary wavelength λ, the complex quantity is not canceled out, and the residual complex quantity is now given by

$$a_r = \delta\phi \frac{a}{2}, \tag{2}$$

where $\delta\phi$, the phase shift between λ and λ_0, is given by

$$\delta\phi = \pi\left(1 - \frac{\lambda_0}{\lambda}\right) \tag{3}$$

TABLE 2
REJECTION FACTOR FOR A MONOCHROMATIC FQPM USED WITH A SPECTRAL BANDWIDTH $\lambda_0 \pm \Delta\lambda/2$

R ($\lambda_0/\Delta\lambda$)	τ (eq. [8])	Numerical Simulations with 10λ
100	48636	46920
50	12156	11732
25	3037	2934
20	1943	1891
10	484	473
7	236	235
5	120	118
3	42	48

with $\phi = 2\pi\delta/\lambda$. The total rejection factor is defined by the relationship $\tau(\lambda) = I/I_r = a^2/a_r^2 = 4/\delta\phi^2$, so, using equations (2) and (3), we found

$$\tau(\lambda) = \frac{4}{\pi^2}\left(\frac{\lambda}{\lambda - \lambda_0}\right)^2. \tag{4}$$

Although the diode wavelength can be tuned from 630 to 640 nm, it is not possible to know in real time its effective wavelength. Then, assuming an FQPM operating wavelength of 628 nm (§ 4.2), the rejection factor may undergo quite a large variation ranging from 1152 to 40,214.

Now, for a spectral bandwidth $\Delta\lambda$, the rejection factor becomes

$$\tau(\Delta\lambda) = 4\Delta\lambda\left[\int_{\lambda_1}^{\lambda_2} d\phi^2\, d\lambda\right]^{-1}, \tag{5}$$

$$\tau(\Delta\lambda) = \frac{4\Delta\lambda}{\pi^2}\left[\int_{\lambda_0-\Delta\lambda/2}^{\lambda_0+\Delta\lambda/2}\left(1 - \frac{\lambda_0}{\lambda}\right)^2 d\lambda\right]^{-1}, \tag{6}$$

$$\tau(\Delta\lambda) = 4\left\{\pi^2\left[1 - \frac{4\lambda_0^2}{\Delta\lambda^2 - 4\lambda_0^2} + 2\frac{\lambda_0}{\Delta\lambda}\ln\left(\frac{2\lambda_0 - \Delta\lambda}{2\lambda_0 + \Delta\lambda}\right)\right]\right\}^{-1}. \tag{7}$$

Let us introduce the spectral resolution $R = \lambda_0/\Delta\lambda$:

$$\tau(\Delta\lambda) = 4\left\{\pi^2\left[1 - \left(\frac{4R^2}{1 - 4R^2}\right) + 2R\ln\left(\frac{2R - 1}{2R + 1}\right)\right]\right\}^{-1}. \tag{8}$$

A second-order Taylor series expansion leads to

$$\tau(\Delta\lambda) \approx \frac{48}{\pi^2}R^2. \tag{9}$$

The theoretical rejection factor would be 490,200 for $\lambda =$ 635 nm and $\Delta\lambda = 2$ nm. Therefore, our measurement ($\tau =$ 4400) is definitely not limited by the source spectral bandwidth but much more by the wavelength shift between the diode and the mask. Table 2 shows the theoretical rejection factor for several spectral resolutions and also gives the results of a numerical simulation using a sum of 10 monochromatic images to generate the bandwidth. These two approaches are in excellent agreement.

5.2. Wave-Front Bumpiness

An important limitation comes from the wave-front bumpiness (high spatial frequencies) of the optical components upstream from the Lyot stop. The lenses L1, L2, and L3 have a standard quality of λ/10 PTV over the full diameter (25.4 mm), which means λ/148 PTV (λ/520 rms) assuming a beam size of only 1.71 mm diameter (the lens quality scales linearly with the beam size). To evaluate the rejection factor, we assume that phase errors are added quadratically. For the three lenses, the total wave-front errors amount to λ/250 to λ/350 rms. With the phase error given by $\delta\phi = 2\pi\delta/\lambda$, we found, using $\tau(\lambda) = a^2/a_r^2$ and equation (2), that

$$\tau(\delta) = \left(\frac{\lambda}{\pi\delta}\right)^2. \tag{10}$$

For an average wave-front bumpiness of $\delta = \lambda/300$, the rejection factor is $\tau(\delta) = 9120$. Therefore, high spatial frequencies may become dominant and result in a wide scattering of the stellar light across the focal plane.

5.3. Source Diameter

Any coronagraphic device is very sensitive to the source diameter, and it is expected that the apparent size of the stellar disk observed with a large telescope in the visible or an interferometer in the thermal infrared would be partially resolved at least for nearby stars ($d < 25$ pc). Therefore, the edge of the stellar disk contributes to a significant fraction of the incoming starlight that leaks through the coronagraph. In our experiment, the fiber has 2 μm in radius equivalent to an angular radius of $0.012\lambda/D$. The radial attenuation of the FQPM is given in Riaud et al. (2002):

$$A(r) = \int_0^r 1 - \exp(-\theta^2/1.16)\, d\theta. \tag{11}$$

This analytical expression was fitted to numerical simulations. Consequently, the rejection factor due to a partially resolved object is given by

$$\tau(r) = \frac{r^2}{2}\left\{\int_0^r [1 - \exp(-x^2/1.16)]x\, dx\right\}^{-1}, \tag{12}$$

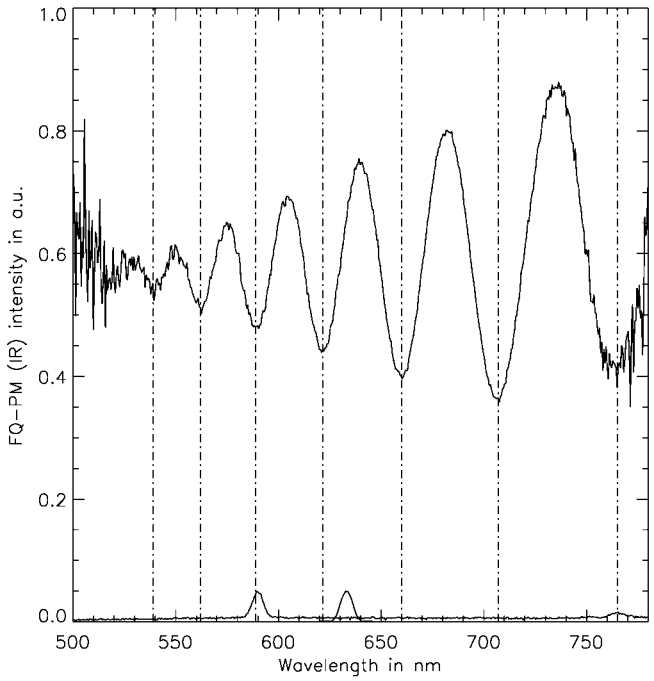

FIG. 8.—Low-resolution spectroscopy of an IR mask operating at 14 μm. Seven orders can be identified from $k = 10$ to $k = 16$ for, respectively, $\lambda = 539$, 562, 589, 621, 660, 707, and 765 nm and allow us to derive accurately an operating wavelength of 14.215 ± 0.004 μm.

with r and x in units of λ/D. As a result, the rejection factor owing to the source diameter is $\tau(r) = 16{,}100$.

5.4. Global Performance

Assuming that these independent errors are added quadratically, the global rejection factor including the wavelength shift, the spectral bandwidth, the wave-front bumpiness, and the source diameter is

$$\tau = \frac{1}{\sqrt{\tau(\lambda)^{-2} + \tau(\Delta\lambda)^{-2} + \tau(\delta)^{-2} + \tau(r)^{-2}}}, \quad (13)$$

$$\tau = 1140\text{–}7785, \quad (14)$$

with a median value $\tau = 3075$. This theoretical value is in fair agreement with our experimental result ($\tau = 4400$) and shows that the dominant source of nulling degradation comes from the wavelength shift between the source and the mask. The upper bound is mainly constrained by the lens quality.

6. DISCUSSION

The laboratory experiment we carried out allows us to fully characterize the intrinsic performance of the FQPM manufactured by SAGEM. We were also able to investigate thoroughly the main causes that limit the nulling performance, such as the spectral range, the wave-front errors, and the source diameter. We performed a quantitative evaluation of these limitations and found that the predictions are in good agreement with experimental results. Better performance is potentially achievable with this optical arrangement if the source wavelength were perfectly matched to the mask operating wavelength. This requires performing a thorough wavelength calibration of both the diode and the FQPM before making any rejection measurements.

In addition, we developed an efficient procedure to accurately determine the operating wavelength of the FQPM with an accuracy of about 1 nm. This technique was useful and evidenced large variations of the mask characteristics with environment conditions. Since the deposited layer is porous, a cleaning of the mask with alcohol temporarily modifies the optical index of this layer, thus shifting the operating wavelength toward the red. To maintain a quite stable optical index, the cleaned mask should be outgassed under vacuum in order to remove any impurities inside the alumina. In that case, we could expect an operating wavelength lower than 628 nm. However, this is a catch-22 situation, since the laser diode is not capable of providing such a wavelength.

The spectroscopic device is also very useful to test the operating wavelength of infrared masks. Indeed, the general relation is

$$\phi = (2k + 1)\pi, \quad (15)$$

where k is an integer. For instance, a mask manufactured in ZnSe ($n = 2.37$) and designed to operate at 14 μm (for $k = 0$) will also provide a π phase shift at 0.621 μm for $k = 13$. Such a measurement was already performed for IR masks at 5 and 14 μm, respectively, in the context of the *James Webb Space Telescope*/Mid-IR Instrument (MIRI) coronagraph (Boccaletti et al. 2003), and a result is shown in Figure 8.

7. CONCLUSIONS AND FUTURE WORK

The FQPM coronagraph experiment we developed demonstrated that a deep extinction of the stellar peak (44,000) and a very low residual speckle level (10^{-7} to 10^{-6}) can be reached with standard-quality lenses. The limitations are various, but the wavelength shift, together with the surface quality, seems to be the most important cause of degradation factors. The spectral bandwidth contributes much less to the degradation of the rejection factor.

In the context of the phase A study for the *James Webb Space Telescope*, we initiated a feasibility study to implement a high-contrast coronagraph inside the MIRI (Dubreuil et al. 2003). Infrared FQPMs have been manufactured and will be tested photometrically under cryogenic temperatures in early 2003 ($T = 55$ K) and 2004 ($T = 7$ K). Numerical simulations (Boccaletti et al. 2003) are promising and show that Jovian planets could be marginally imaged at thermal wavelengths, thus allowing the measurement of the effective temperature of

the planet and subsequently the derivation of its mass through appropriate models.

Another study has started for ground-based facilities using extreme adaptive optics (Strehl ratio ≈0.9). Our team is contributing to a European consortium to address the feasibility of a planet-finder instrument for the VLT (ESO). Near-IR FQPMs will be manufactured and tested in that study phase (2003 March to 2004 August). In that particular case, we will also investigate the use of half-wave plates and zero-order gratings to provide an achromatic phase shift in the near-IR from 0.7 to 2.5 μm with a single FQPM (Mawet et al. 2003).

The use of an FQPM coronagraph on a space interferometer to search for terrestrial planets is also envisaged, but it requires an achromatic phase mask (better than 5×10^{-3} radians rms) over a large bandwidth (7–25 μm) and low residual wave-front errors. A complete study was performed by Riaud et al. (2002) to demonstrate the performance of an FQPM with a densified-pupil interferometer in space (Labeyrie 1996).

REFERENCES

Boccaletti, A., Riaud, P., & Rouan, D. 2002, PASP, 114, 132
Boccaletti, A., Riaud, P., Rouan, D., & Baudrand, J. 2003, Proc. SPIE, 4850, 556
Dubreuil, D., et al. 2003, Proc. SPIE, 4850, 564
Guyon, O., et al. 1999, PASP, 111, 1321
Labeyrie, A. 1996, A&AS, 118, 517
Lyot, B. 1939, MNRAS, 99, 580
Mawet, D., Lenaerts, C., Moreau, V., Renotte, Y. L. M., Rouan, D., & Surdej, J. 2003, Proc. SPIE, 4860, 182
Riaud, P., Boccaletti, A., Rouan, D., Lemarquis, F., & Labeyrie, A. 2001, PASP, 113, 1145
Riaud, P., et al. 2002, A&A, 396, 345
Roddier, F., & Roddier, C. 1997, PASP, 109, 815
Rouan, D., Boccaletti, A., Riaud, P., & Baudrand, J. 2003, Proc. SPIE, 4860, 192
Rouan, D., Riaud, P., & Baudrand, J. 2002, in Proc. ESO Conf. 58, Beyond Conventional Adaptive Optics, ed. E. Vernet, R. Ragazzoni, S. Esposito, & N. Hubin (Garching: ESO), 193
Rouan, D., Riaud, P., Boccaletti, A., Clénet, Y., & Labeyrie, A. 2000, PASP, 112, 1479